Remote Sens. **2011**, *3*, 1914-1942; doi:10.3390/rs3091914

OPEN ACCESS

Remote Sensing

ISSN 2072-4292

www.mdpi.com/journal/remotesensing

Article

AMARTIS v2: 3D Radiative Transfer Code in the [0.4; 2.5 µm] Spectral Domain Dedicated to Urban Areas

Colin Thomas [1,2,*], Stéphanie Doz [1,2], Xavier Briottet [1] and Sophie Lachérade [3]

[1] Onera, The French Aerospace Lab, 2 avenue Edouard Belin, BP 4025, 31055 Toulouse Cedex 4, France; E-Mails: stephanie.doz@dga.defense.gouv.fr (S.D.); xavier.briottet@onera.fr (X.B.)

[2] ISAE, Université de Toulouse, 10 avenue Edouard Belin, BP 54032, 31055 Toulouse Cedex 4, France

[3] CNES, 18 avenue Edouard Belin, 31401 Toulouse Cedex 9, France; E-Mail: sophie.lacherade@cnes.fr

* Author to whom correspondence should be addressed; E-Mail: colin_thomas@ymail.com; Tel.: +33-6-8320-5011.

Received: 3 July 2011; in revised form: 23 August 2011 / Accepted: 23 August 2011 / Published: 31 August 2011

Abstract: The availability of new very high spatial resolution sensors has for the past few years allowed a precise description of urban areas, and thus the settlement of specific ground or atmosphere characterization methods. However, in order to develop such techniques, a radiative transfer tool dedicated to such an area is necessary. AMARTIS v2 is a new radiative transfer code derived from the radiative transfer code AMARTIS specifically dedicated to urban areas. It allows to simulate airborne and spaceborne multiangular observations of 3D scenes in the [0.4; 2.5µm] domain with the ground's geometry, urban materials optical properties, atmospheric modeling and sensor characteristics entirely defined by the user. After a general presentation of AMARTIS v2 and a description of the performed calculations, results of radiometric intercomparisons with other radiative transfer codes are presented and the new offered potentials are illustrated with four realistic examples, representative of current issues in urban areas remote sensing.

Keywords: AMARTIS; radiative transfer; urban area; remote sensing; 3D; reflective domain

---

1. Introduction

The study of urban areas is becoming an important challenge as most of the population in the world is concentrated in such areas (about 3 billion people in 2000, representing about 40% of world's population [1]). The analysis of its growth [2-4] and its impact on the climate change [4] are the focus of a lot of scientific development [5-8]. The advent of new multispectral and hyperspectral high spatial resolution sensors operating in the visible and the near infrared spectra offers the possibility of considerably improving the study of urban areas. Indeed, airborne sensors like PELICAN [9] and satellite sensors like Quickbird [10], Ikonos [11] and PLEIADES [12] allow for instance the improvement of urban area mapping at the local scale [13-15], material identification [5] and even aerosols optical properties retrieval [16-18].

However, developing such methods at high spatial resolution is difficult because urban areas have very diverse geometries and because their radiative properties must be taken into account. Indeed, urban areas have specific relief especially due to the man-made buildings. Those constructions imply a change of the irradiance at ground level by occulting the direct signal and then creating shadows (Figure 1), and by screening the scattered and the Earth-atmosphere coupling irradiances. The decrease of the irradiance at ground level by those screening effects is however partially compensated by another radiative effect: the reflection of light by buildings. The amount of this component of the at-ground-level signal depends directly on the spectral optical properties of the materials constituting the environment: their reflecting capabilities and their bidirectional behaviors. The radiances measured by the sensor depend on the optical properties of the considered surfaces, but also on their slopes. These slope effects can easily be observed on urban area images as shown in Figure 1.

Figure 1. Image of Toulon (France) acquired by PELICAN multispectral sensor at a 20 cm spatial resolution.

To develop new characterization methods of physical parameters of urban areas from at-sensor radiance measurements, it is mandatory to understand and evaluate all the radiative processes present in such complex medium. To this end, a radiative transfer tool adapted to urban areas must be used. Some radiative transfer codes exist but, unfortunately, are not adapted to such works. Well known codes like 6S [19] or MODTRAN [20] can simulate simple heterogeneous scenes but are limited to flat

landscapes with a homogeneous environment. Although COMANCHE [21,22] offers improvements by better modeling the Earth-atmosphere coupling irradiance using Monte Carlo methods which allow considering complex heterogeneous landscapes, the flat surface assumption still remains. For urban areas, the 3D structure of the landscapes needs to be taken into account. DART [23] can achieve such simulations but its main drawback is that it does not give access to all radiative terms at surface and sensor levels, which are essential to conduct radiative phenomenological studies. AMARTIS v1 (Advanced Modelling of the Atmospheric Radiative Transfer for Inhomogeneous Surfaces [24-26]) has been developed to this end. It can simulate every radiative contributor on these two levels. Unfortunately, it is limited by the description of the landscape, defined by a 2D profile which is infinitely reproduced in the third dimension. Secondly, each urban surface, like roofs, walls and roads, is considered as uniform with unique optical properties. Furthermore, the aerosol distribution can only be described by a Junge law [27] whereas Thomas *et al.* [28] has shown the high variability of urban aerosols radiative properties.

Therefore, in order to overcome these limitations a new radiative transfer code derived from AMARTIS v1 has been developed, taking into account a real 3D description of the landscape, each scene element being defined by its spectral bidirectional reflectance. The atmosphere modeling has also been improved with the addition of new aerosol models. This tool is also now able to perform the simulation and the visualization of synthetic remote sensing images.

This paper aims to present this new tool: AMARTIS v2. In a first step, a description of the code is given (Section 2), then a comparison of its radiometric performances with other radiative transfer codes is detailed (Section 3). Finally, its new potentialities are illustrated with four examples: study of the radiative transfer for an urban canyon (Section 4.1), analysis of the impact of highly reflective windows in a shadowed canyon street (Section 4.2), comparison of the signal coming from an irradiated area and those from a shaded area in the case of a complex landscape (case of a crossroad, Section 4.3), and finally, evaluation of the directional effects induced on the at-sensor level signal by an urban canyon when using broader resolution at a street scale (Section 4.4). Conclusions and perspectives are then discussed (Section 5).

2. Description of the 3D Radiative Transfer Code AMARTIS v2

2.1. General Description

AMARTIS v2 [29] aims to remove the drawbacks of the previous code AMARTIS v1. Its main functionalities, *i.e.*, scene description, sensor and atmosphere characteristics and radiative transfer modeling, are discussed below.

This code performs monochromatic radiative transfer computations in the [0.4; 2.5 μm] spectral domain. Its inputs are the geometry and the materials optical properties of a 3D scene, the atmospheric properties and the viewing and irradiating conditions. It computes all the radiative components of the signal, both at ground level (irradiance) and at sensor level (radiance) at every point of the landscape. Thus, it can simulate the radiance image of the scene acquired by the sensor.

AMARTIS v2 uses 6S [19] to model the radiative transfer above the canopy level. Thus, like 6S, the gaseous absorption (quantified by the gaseous transmission T_g) is separated from the other radiative effects of the atmosphere outside the strong absorption bands.

As explained previously, AMARTIS v2 is based on the radiative transfer code AMARTIS v1. However, very important changes have been performed and will be described in the next sections of the document. The main improvements in comparison to AMARTIS v1 are:

- The more realistic description of the atmosphere thanks to the coupling with 6S, especially the availability of new optical and geophysical aerosol models.
- The possibility of modeling realistic complex 3D scenes.
- The huge decrease of the computation time thanks to the use of an efficient ray-tracing tool for the Monte Carlo calculations.

2.2. Inputs Description

2.2.1. Scene

The scene is defined by its geometry and its radiative properties. A synthetic 3D scene of rectangular basis is used as input of AMARTIS v2. It is composed of uniform triangular-shaped facets. The scene can be built using the Google Sketch' Up tool (http://sketchup.google.com), or defined by available vector elevation models (VEM) of real landscapes. In any case, it has to be triangulated.

The facet represents the surface unit for the irradiances calculations. The definition of the facet size must allow a good signal reconstitution and a reasonable computation time. Each facet is considered homogeneous in terms of optical properties, here the reflectance. Each facet reflectance can have either lambertian or bidirectional behavior. The physical description consists in associating a facet with its reflectance model. The mathematical descriptions of these models are implemented in AMARTIS v2. Some bidirectional optical properties were already used in AMARTIS v1 but were very limited. Now any model can be easily integrated in AMARTIS v2 like Phong's model [30], Cook-Torrance's model [31] or Snyder's model [32].

The sun and sensor directions are defined in the coordinates system associated to the XYZ reference system defined in Figure 2.

Figure 2. Definition of the zenith and azimuth angles of the sensor (θ_V, φ_V) and of the sun (θ_S, φ_S).

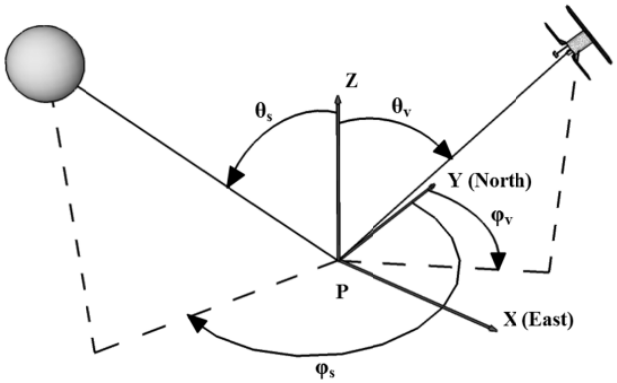

2.2.2. Atmosphere

The atmospheric radiative properties are modeled in AMARTIS v2 thanks to the radiative transfer code 6S [19]. The aerosols can be modeled by the standard models of 6S, by their physical properties (with notably Junge or multimodal distributions) or directly by their optical properties (spectral variation of the optical thicknesses, single scattering albedos and phase functions). The gaseous atmosphere can be modeled by the standard models of 6S or by the ozone and water vapor contents.

2.2.3. Sensor

AMARTIS v2 allows the simulation of airborne or satellite sensors. The sensor is defined by the following parameters: its zenith and azimuth viewing angles defined by the optical axis orientation pointed at the centre of the scene, its pixels matrix (number of pixels by rows and columns and pixel size), its spatial resolution, the wavelengths of observation (AMARTIS v2 simulates monochromatic observations), and the focal length of the instrument. The altitude of the sensor is deduced from the previous geometrical parameters. The modeled instrument has a perfect signal-to-noise ratio corresponding to no instrumental noise.

2.3. Method Description

In remote sensing, a flat ground assumption is usually made to model the signal at ground and sensor levels. However, in cities, at very high spatial resolution, this hypothesis is no longer valid because of the complexity introduced by the relief which induced specific radiative effects. Thus, it becomes necessary to use a new formalism adapted to those areas. The signal at ground and at sensor levels is the result of several radiative components as described in Figure 3 ([24,25]).

The irradiance at ground level (I_{tot}) is the sum of four components (Figure 3(a)): the direct irradiance (I_{dir}), the scattered irradiance (I_{scat}), the Earth-atmosphere coupling irradiance (I_{coup}) and the downward reflected irradiance (I_{refl}). The radiance at sensor level (R_{tot}) is the sum of three components (Figure 3(b)): the direct radiance (R_{dir}), the environment radiance (R_{env}) and the atmospheric radiance (R_{atm}).

The formalism and the radiative calculations performed in AMARTIS v2 are the same as in AMARTIS v1, except for I_{scat} and R_{atm}.

Their expressions are now detailed but to avoid complications, the wavelength dependence has been omitted in the formulations.

The direct irradiance corresponds to the photons directly coming from the sun, and is defined for a point P at ground level by [33]:

$$I_{dir}(P) = I_{TOA} < \vec{N}(P).\vec{n}_S > T_g^{\downarrow}(P,\theta_S)\exp(-\frac{\tau^{\downarrow}(P)}{\cos(\theta_S)})bool(P,\theta_S,\varphi_S) \quad (1)$$

with I_{TOA} the top of the atmosphere solar irradiance (in $W.m^{-2}.\mu m^{-1}$), $< \vec{N}(P).\vec{n}_S >$ the scalar product of $\vec{N}(P)$ (unit vector normal to the ground at the point P) and $\vec{n}_S$ (unit vector directed from P to the sun), $T_g^{\downarrow}(P,\theta_S)$ the gaseous transmission of the atmosphere between the top of the atmosphere and P, $\tau^{\downarrow}(P)$ the optical thickness of the total atmosphere column (aerosols and molecules), θ_S and φ_S the zenith

and azimuth angles of the sun, and $bool(P,\theta_S,\varphi_S)$ a Boolean factor equal to 1 if P is in the sun and to 0 if P is in the shade.

Figure 3. Components of the irradiance at ground level (**a**) and of the radiance at sensor level (**b**). The direct irradiance (I_{dir}) corresponds to the photons coming directly from the sun, the scattered irradiance (I_{diff}) to the photons scattered by the atmosphere, the Earth-atmosphere coupling irradiance (I_{coup}) to the photons resulting from multiple surface reflections and atmospheric scatterings, and the downward reflected irradiance (I_{refl}) to the photons that are directly transmitted to the ground after reflection from the neighborhood. The direct radiance (R_{dir}) corresponds to the photons coming from the surface directly; the environment radiance (R_{env}) to the photons coming from the surface after scattering by the atmosphere; and the atmospheric radiance (R_{atm}) to the photons that have been scattered by the atmosphere without reaching the surface.

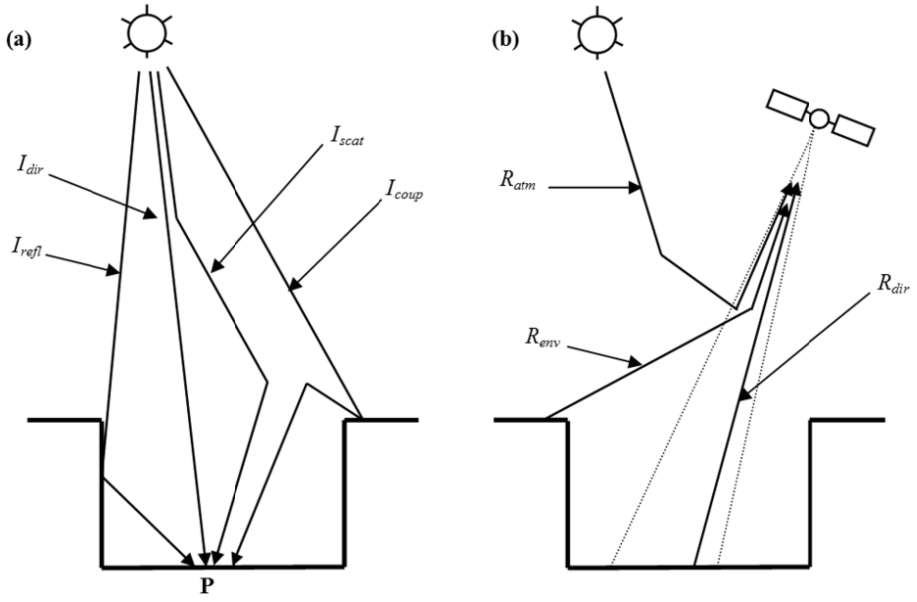

The scattered irradiance corresponds to the photons scattered by the atmosphere and incident on point P. It is defined by [33]:

$$I_{scat}(P) = T_g^{\downarrow}(P,\theta_S) \iint_{\Omega_{sky}} R_{sky}^{d}(\theta,\varphi)\cos(\theta)d\omega \ \text{(in W.m}^{-2}\text{.µm}^{-1}\text{)} \tag{2}$$

with $R_{sky}^{d}(\theta,\varphi)$ the radiance scattered by the sky in the direction defined by the zenith angle θ and azimuth angle φ (in W.m^{-2}.µm^{-1}.sr^{-1}), $T_g^{\downarrow}(P,\theta_S)$ the gaseous transmission of the atmosphere between the top of the atmosphere and P, and Ω_{sky} the solid angle of sky view at point P.

The gaseous transmission taken into account in Equation (2) is the gaseous transmission between the top of the atmosphere and the point P. The photons scattered by the atmosphere and reaching the ground at point P have a longer path in the atmosphere that should increase this transmission. However, Miesch [33] has shown that this approximation is realistic outside strong absorption bands and we have chosen to use it in AMARTIS v2 as in AMARTIS v1.

The Earth-atmosphere coupling irradiance corresponds to the photons resulting from multiple surface reflections and atmospheric scatterings whereas the downward reflected irradiance corresponds

to the photons directly transmitted to the ground after reflections from the neighborhood. The Earth-atmosphere coupling irradiance cannot be expressed by an analytical formulation because of the complex geometry of the scene. This is the reason why this component is computed by means of Monte Carlo methods [25]. The downward reflected irradiance might be calculated by an analytical method. This has not been selected as the Earth-atmosphere coupling computation simultaneously calculates the downward reflected irradiance. This Monte Carlo principle consists of modeling the radiometric flux by analyzing the propagation of a high number of photons (usually ~10^9 to 10^{10} per simulation) in the Earth-atmosphere system. The phenomena of scattering and absorption by the atmosphere and of reflection and absorption by the ground are modeled by statistical laws [25]. As the Earth-atmosphere coupling irradiance and the downward reflected irradiance result from interactions with the ground, the neighborhood of the scene has an impact on the signal. As it is not modeled by the 3D scene, this impact is calculated by duplicating virtually the original scene. A comparable approach was implemented in AMARTIS v1 [33]. As the ray-tracing was not implemented, a method by photon propagation was used. Now, the introduction of the ray-tracer RayBooster (http://www.hpc-sa.com) has considerably improved the computation time.

The direct radiance corresponds to the photons reflected by the surface directly toward the sensor. It is defined by:

$$\begin{aligned} R_{dir}(i) &= R_{dir}^{dir}(i) + R_{dir}^{scat}(i) + R_{dir}^{coup\_refl}(i) \\ &= \frac{1}{\Omega_i}\iint_{\Omega_i}[I_{dir}(S_{d\omega})\rho^{dd}(S_{d\omega})]\frac{T_{dir}^{\uparrow}(S_{d\omega})}{\pi}d\omega \\ &+ \frac{1}{\Omega_i}\iint_{\Omega_i}[T_g^{\downarrow}(P,\theta_S).\iint_{\Omega_{sky}} R_{sky}^{d}(\theta,\varphi)\cos(\theta)\rho^{dd}(S_{d\omega})d\omega]\frac{T_{dir}^{\uparrow}(S_{d\omega})}{\pi}d\omega \ \text{(in W.m}^{-2}\text{.µm}^{-1}\text{.sr}^{-1}\text{)} \\ &+ \frac{1}{\Omega_i}\iint_{\Omega_i}[(I_{coup}(S_{d\omega}) + I_{refl}(S_{d\omega}))\rho^{hd}(S_{d\omega})]\frac{T_{dir}^{\uparrow}(S_{d\omega})}{\pi}d\omega \end{aligned} \quad (3)$$

where R_{dir}^{dir}, R_{dir}^{scat}, and $R_{dir}^{coup\_refl}$ are respectively the contributions to the direct radiance resulting from the direct irradiance, the scattered irradiance and the coupling and reflected irradiances; Ω_i is the solid angle corresponding to the field of view of the pixel i; $S_{d\omega}$ is the surface at ground level seen by this pixel in the direction of $d\omega$; $R_{sky}^{d}(\theta,\varphi)$ is the radiance scattered by the sky in the direction defined by the zenith angle θ and azimuth angle φ (in W.m^{-2}.µm^{-1}.sr^{-1}); $T_{dir}^{\uparrow}(S_{d\omega})$ is the direct transmission of the atmosphere between $S_{d\omega}$ and the sensor; ρ^{dd} is the bidirectional reflectance of the corresponding material; and ρ^{hd} its hemispheric-directional reflectance.

For lambertian materials, Equation (3) becomes:

$$R_{dir}(i) = \frac{1}{\Omega_i}\iint_{\Omega_i} I_{tot}(S_{d\omega})\rho(S_{d\omega})\frac{T_{dir}^{\uparrow}(S_{d\omega})}{\pi}d\omega \ \text{(in W.m}^{-2}\text{.µm}^{-1}\text{.sr}^{-1}\text{)} \quad (4)$$

with ρ the lambertian reflectance.

The environment radiance, R_{env}, corresponds to the photons coming from the surface and scattered by the atmosphere. As for the Earth-atmosphere coupling irradiance, this term cannot be modeled by an analytic expression and is also solved with Monte Carlo calculations [25].

The atmospheric radiance, R_{atm}, corresponds to the photons that have been scattered by the atmosphere without reaching the ground and is directly calculated thanks to the radiative transfer code 6S.

Thus, AMARTIS v2 allows the computation of the incident irradiances to the ground as described above (I_{dir}, I_{scat}, I_{coup} and I_{refl}) and of the sum of those components (I_{tot}) for each facet of the scene. Whereas irradiances are calculated for each facet, radiances are calculated for each pixel. In order to represent these different irradiances at the sensor resolution and to model the at sensor radiances, the different irradiances incident to a given facet must be aggregated. Each irradiance type incident to a ground pixel is the sum of the corresponding irradiance type incident to each facet included in this ground pixel and weighted by the solid angle defined by this facet. The sum of these solid angles equals the instantaneous field of view of a pixel.

The radiances at sensor level (R_{dir}, R_{atm} and R_{env}) are directly calculated for each pixel and their sum will simulate the synthetic image acquired by the sensor (R_{tot}). Therefore, all the radiative components of the signal can be represented on different images.

To perform these calculations, the following atmospheric radiative terms are directly derived from 6S: R_{atm}, $T_{dir}^{\uparrow}$, $T_{g}^{\downarrow}$, R_{sky}^{d}, $\tau^{\downarrow}$.

3. Comparison of AMARTIS v2 with Existing Radiative Transfer Codes

The potentialities of AMARTIS v2 are unique. Indeed, it allows both the use of complex 3D scenes and a large modeling of the atmosphere. This is the reason why the comparison between AMARTIS v2 and existing radiative transfer codes should be limited. Nevertheless, major efforts have been done in order to estimate its performances. A comparison has been performed, first with AMARTIS v1 to assess they provide the same results on simple cases, and then with 6S to validate the atmospheric modeling.

3.1. Comparison with AMARTIS v1

AMARTIS v2 is first compared with AMARTIS v1 to check the coherence of those two codes. As AMARTIS v1 can only take into account simple 3D scenes and is limited in atmospheric modeling, the comparison procedure is restrained to conditions AMARTIS v1 can simulate.

This comparison is performed for the different radiative components of the signal. However, different atmospheric scattering models are used in AMARTIS v1 and v2. Indeed, in AMARTIS v1, a Gauss-Seidel model [34] is used whereas in AMARTIS v2, the 6S kernel used performs different analytical calculations based on the successive orders of scattering [19]. Thus, the scattered irradiance and the atmospheric radiance are not compared.

Two different synthetic landscapes are chosen (Figure 4): an urban canyon and a mountainous scene. The modeled grounds are considered as lambertian with spectrally constant reflectances ρ. For each scene, two different reflectance configurations are defined (Figure 4). Those scenes are observed in nadir viewing by a sensor onboard an aircraft flying at 2.25 km altitude with a spatial resolution of 10 cm. The sun has a zenith angle of 30° and is located in a plan perpendicular to the street and the valley axis. The simulations are performed at 440, 870 and 1,600 nm. The atmosphere is modeled by the standard "mid-latitude summer" model of 6S for the molecules and by a Junge distribution [27] for the aerosols. This distribution is defined by particles of radius ranging from 0.01 to 10 μm, with a refractive index of 1.35 + 0.007*i*, spectrally constant in the [0.4; 2.5 μm] domain and with a Junge parameter of 3.32. Their abundances are defined from the following visibilities: 5 km and 23 km.

Figure 4. Geometry and reflectances of the scenes used to compute the comparison simulations between AMARTIS v1 and AMARTIS v2: street configuration **(a)** and mountainous configuration **(b)**.

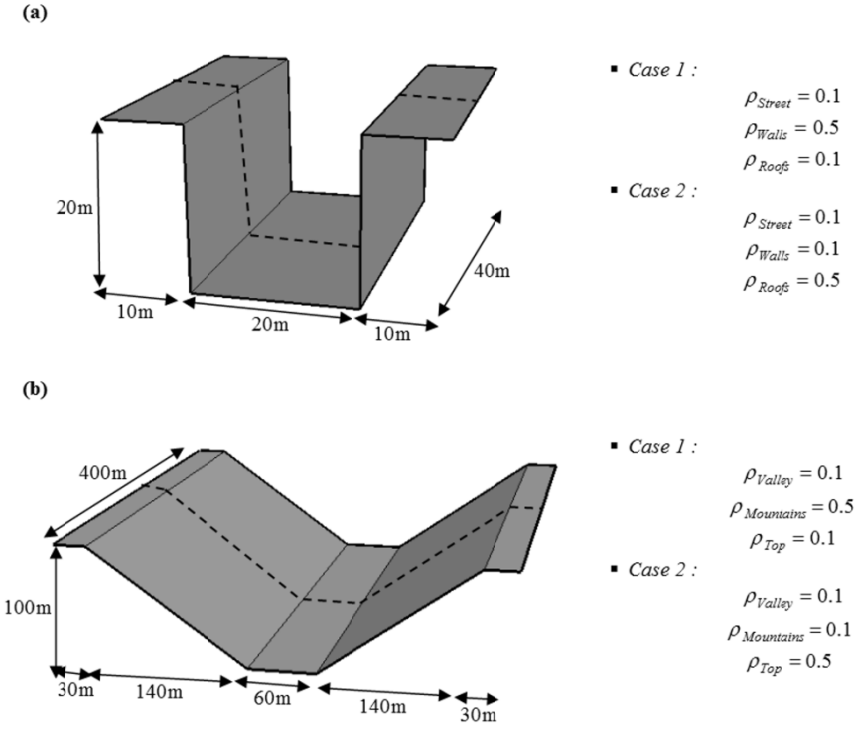

The results are compared using the mean relative quadratic error *Er* which is first calculated for each component of the signal *C* and for each simulation *s* (depending on the geometry, the reflectance configuration, the wavelength and the visibility of the atmosphere). It is estimated, from the values $C_{v1}(i)$ and $C_{v2}(i)$ respectively obtained from AMARTIS v1 and v2 for *n* equidistant points of a transect represented as a dashed line in Figure 4, as:

$$Er_s = \sqrt{\frac{\sum_{i=1}^{n} \left(\frac{C_{v1}(i) - C_{v2}(i)}{C_{v1}(i)}\right)^2}{n}} \tag{5}$$

The parameter *n* equals 40 except when some values of C_{v1} equal 0. In this case, these points are not taken into account for the calculation of *Er*. These null values correspond to points in shadow (in the case of the street) for the direct irradiance and to the points on the roofs and on the top of the mountains (Figure 4) for the downward reflected irradiance. *n* is always superior or equal to 20.

From all those simulations, an average of the mean relative quadratic errors $\overline{Er}$ and its corresponding standard deviation is deduced for each component of the signal. It quantifies the mean relative difference obtained between those two codes.

The results obtained for the components we want to compare (I_{dir}, I_{coup}, I_{refl}, R_{dir} and R_{env}) are presented in Table 1. As the differences obtained for I_{scat} because of the different atmosphere scattering models has an impact on the total signal at ground level, the total irradiance at ground level I_{tot} has also been added to the table. Indeed it allows directly assessing the impact of the different scattering models on R_{dir} and R_{env}, and at the first order on I_{coup} and I_{refl} because those two components depend on the sum of I_{dir} and I_{scat}. Examples of simulation results are also given in Figure 5 to observe the spatial

variations of the signal. The case chosen here is the mountainous case No. 2 (*cf.* Figure 4) observed at 870 nm with a visibility of 23 km. Other illustrations of Monte Carlo simulations are presented in Figure 6. It corresponds to the results obtained for I_{coup} and I_{refl} in the street case No. 1 (*cf.* Figure 4) observed at 440 nm with a visibility of 5 km.

Table 1. Mean relative quadratic error for each radiative component $\overline{Er}$ obtained from AMARTIS v2 compared to AMARTIS v1 and corresponding standard deviations.

Radiative component	$\overline{Er}$	σ
I_{dir}	0.0%	0.0%
I_{coup}	8.9%	5.3%
I_{refl}	6.8%	3.4%
I_{tot}	2.8%	1.5%
R_{dir}	2.9%	1.4%
R_{env}	3.0%	1.5%

Figure 5. Comparison of simulation results obtained with AMARTIS v1 (thin line) and AMARTIS v2 (thick line) in the mountainous case No. 2 (*cf.* Figure 4) at 870 nm with a visibility of 23 km. The reflectance of the ground is 0.1 except at the top of the relief where it is 0.5.

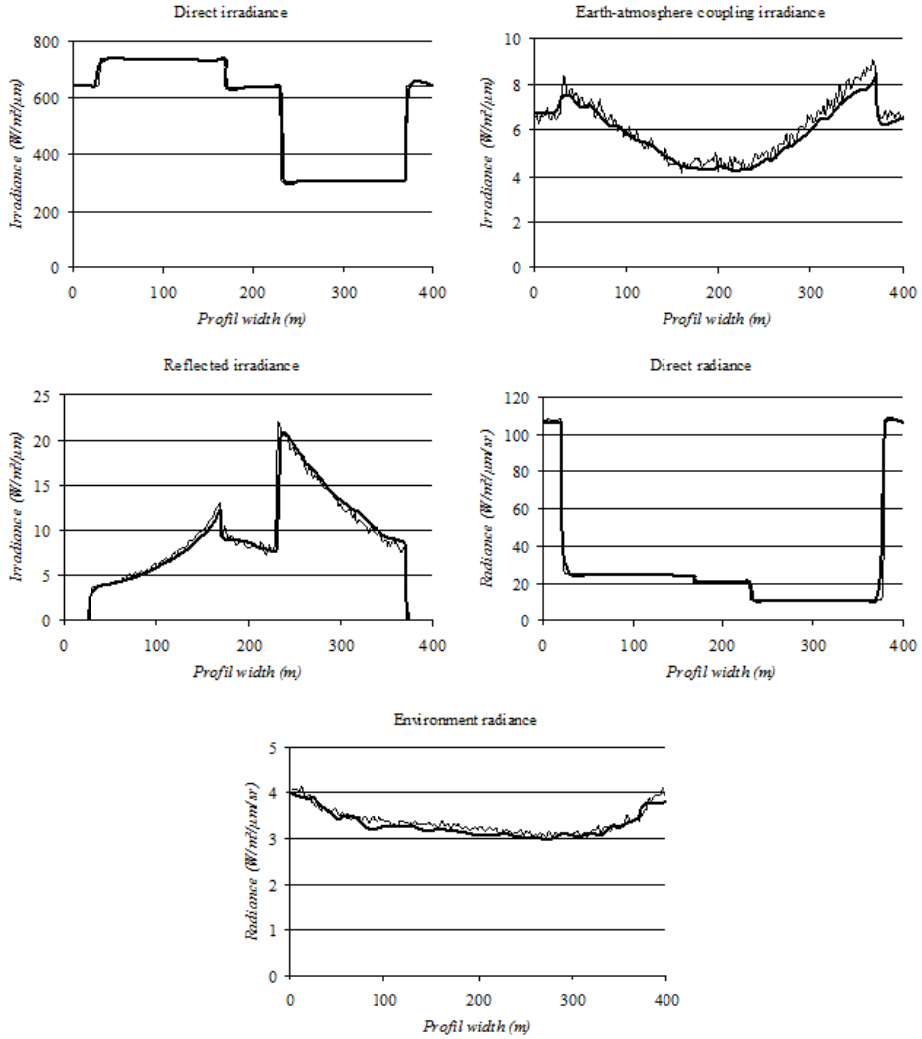

As can be noted in Table 1 and in Figure 5, these results are in very good agreement. The values of the direct irradiances are equal because their analytical expressions used in the two codes are identical. The direct and environment radiances show some small discrepancies that are directly due to the difference of total irradiance at ground level resulting from the different atmospheric scattering models: mean difference of 3% between AMARTIS v2 and AMARTIS v1 for those three terms.

The Earth-atmosphere coupling irradiances and the downward reflected irradiances exhibit higher discrepancies, up to 8.9% in the case of I_{coup}. Those differences are due to two reasons. First, as previously, a part of those discrepancies are due to the difference of scattered irradiance at ground level. This can have a huge impact on the calculation of I_{coup} and I_{refl} notably in the street cases where the presence of shadows (areas where the direct irradiance is null) increases the relative contribution of the scattered irradiance. However, this is not the only reason. As can be seen in Figure 5 and especially in Figure 6, the other reason is the noisy signal resulting from AMARTIS v1 simulations. This noisy signal is due to the use of fewer photons for the Monte Carlo calculations in AMARTIS v1 than in AMARTIS v2. Indeed, AMARTIS v2 allows obtaining a very good convergence of the components calculated with Monte Carlo techniques by simulating the propagation of numerous photons (~10^{10} per simulation) in the atmosphere. This is possible thanks to the efficient ray-tracing tool that allows obtaining reasonable computation times (~1 h per simulation). The Monte Carlo methods of AMARTIS v1 are implemented in a way that makes the computations very slow compared to AMARTIS v2. Thus, it has not been possible to simulate the propagation of as many photons (less than 10^9 per simulation) because of the long computation times (up to 12 h per simulation in this case) and therefore we have obtained a less good convergence of I_{coup}, I_{refl} and R_{env}.

Figure 6. Comparison of simulation results obtained with AMARTIS v1 (thin line) and AMARTIS v2 (thick line) in the street case No. 1 (*cf.* Figure 4) at 440 nm with a visibility of 5 km.

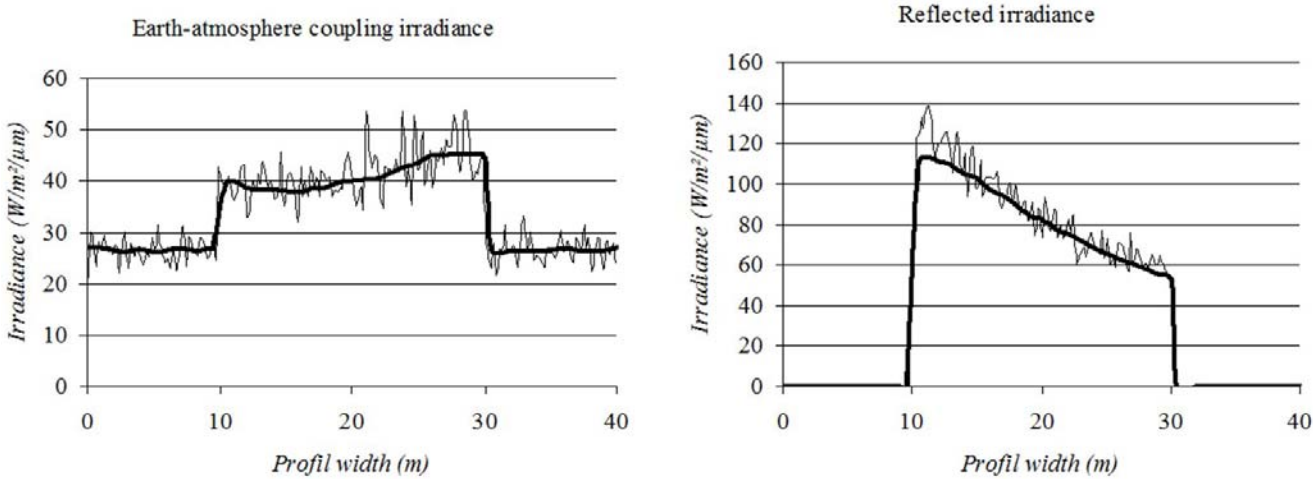

Finally, it is interesting to note in Figures 5 and 6 that the components of the signal have the same spatial variations in AMARTIS v2 simulations as in AMARTIS v1 simulations, thanks to the precise ray tracing software used to handle the geometry of the code.

3.2. Comparison with 6S

AMARTIS v2 has been compared with 6S for flat grounds to check both the correct use of 6S in AMARTIS v2 as a radiative transfer tool above canopy level and the atmospheric modeling.

In AMARTIS v2, I_{dir}, I_{scat}, R_{dir} and R_{atm} are calculated in the same way as in 6S or result from 6S calculations. So, the two codes should give similar results for those radiative components. However, it is necessary to check it. Then, as the I_{coup}, I_{refl} and R_{env} components are calculated with different methods, a comparison has to be done.

To do so, a scene of lambertian reflectance 0.2 (spectrally constant) is used. A nadir satellite viewing is simulated at 440, 870 and 1,600 nm with a solar zenith angle of 30° and a molecular atmosphere modeled with the "mid-latitude summer" model. Four aerosols distributions are used, defined by spectrally constant single scattering albedos and asymmetry factors. The values of those parameters are presented in Table 2. The phase functions of aerosols distributions are defined by the Henyey-Greenstein function [35]. The concentrations of those particles are described by two visibilities: 5 km and 23 km. Another case is also computed corresponding to an atmosphere without aerosols.

Table 2. Single scattering albedos and asymmetry factors of the 4 aerosols models used for the comparison between AMARTIS v2 and 6S.

Aerosols models	Single scattering albedo	Asymmetry factor
M1	0.6	0.6
M2	0.6	0.9
M3	0.9	0.6
M4	0.9	0.9

In all, 27 simulations were performed both with AMARTIS v2 and 6S. The mean value of the absolute differences and the corresponding standard deviations obtained with 6S and for the central pixel of the images computed by AMARTIS v2 were calculated and presented in Table 3. To be able to assess the impact of the discrepancies on the total signal at ground and sensor levels, the mean differences and their standard deviation normalized by I_{tot} for the irradiances and by R_{tot} for the radiances are also presented. Finally, in order to have the order of magnitude of the different components of the signal, the minimum, mean and maximum values obtained with the AMARTIS v2 simulations have been added to this table.

As expected, the results obtained for analytical calculations (I_{dir}, I_{scat}, R_{dir} and R_{atm}) are identical with mean discrepancies compared to the total signal of 0.0% except for R_{dir} where a slight difference of 0.2% is obtained. This is explained by the difference obtained for the total signal at ground level due to the discrepancy on the Earth-atmosphere coupling irradiance. For the environment radiance, the mean difference compared to the total radiance is 0.8%, corresponding to a mean absolute error of 0.5 $W.m^{-2}.\mu m^{-1}.sr^{-1}$. For the Earth-atmosphere coupling irradiance, the mean difference compared to the total irradiance is 0.4%, corresponding to a mean absolute error of 3.3 $W.m^{-2}.\mu m^{-1}$. Those components are the ones that show the maximum discrepancies in absolute level with 6S because of the different calculation methods (analytical calculations for 6S, Monte Carlo calculations for AMARTIS v2). However, as can be noticed in Table 3, they are also the components that contribute

the least to the total signal at ground and sensor levels and those differences have very little impact on the signal modeling.

Table 3. Comparison of the results obtained between AMARTIS v2 and 6S on the 27 simulation cases.

	AMARTIS v2 values ($W.m^{-2}.\mu m^{-1}$)			**Difference between AMARTIS v2 and 6S**			
				Absolute difference ($W.m^{-2}.\mu m^{-1}$)		**Difference normalized by I_{tot}**	
	Min	Mean	Max	Mean	Standard deviation	Mean	Standard deviation
I_{dir}	171.80	474.06	1,132.67	0.23	0.33	0.03%	0.03%
I_{scat}	0.14	175.51	746.00	0.01	0.00	0.00%	0.00%
I_{coup}	0.06	17.40	60.43	3.34	4.06	0.42%	0.37%
I_{tot}	188.85	666.98	1,348.58	3.46	4.23	0.43%	0.39%

	AMARTIS v2 values ($W.m^{-2}.\mu m^{-1}$)			**Difference between AMARTIS v2 and 6S**			
				Absolute difference ($W.m^{-2}.\mu m^{-1}$)		**Difference normalized by R_{tot}**	
	Min	Mean	Max	Mean	Standard deviation	Mean	Standard deviation
R_{dir}	10.11	27.38	67.26	0.12	0.12	0.21%	0.16%
R_{atm}	0.04	18.33	84.05	0.00	0.00	0.01%	0.01%
R_{env}	0.01	7.27	30.24	0.54	0.75	0.90%	0.84%
R_{tot}	11.26	52.97	121.53	0.43	0.67	0.74%	0.71%

Finally, good agreements were obtained between 6S and AMARTIS v2 for flat ground simulations, proven by the very low difference for the total signals at sensor level, with a mean value of 0.4 $W.m^{-2}.\mu m^{-1}.sr^{-1}$ corresponding to a relative value of 0.7%.

4. Illustrations of the Improvements Brought by AMARTIS v2

As explained previously, AMARTIS v2 is a radiative transfer tool that allows the calculation of all the components of the signal with a good accuracy (*cf.* previous section) and their representation. It notably allows the simulation of the radiance image of the scene acquired by the sensor.

To illustrate the gain brought by this code compared to AMARTIS v1 and to present its new potentialities, four examples are presented. First, a simulation of the observation of an urban canyon is detailed. Then, the use of materials exhibiting high directional reflection behaviors is presented with the example of the specular reflection of light by window panes. A radiative analysis of the signal in sunny and shady areas in the case of a crossroad follows. Finally, the aggregation process over a heterogeneous landscape is presented in the case of a street pattern and the directional effects induced by this aggregation are evaluated.

Note that the geometric accuracy of AMARTIS v2 is a major issue for such complex 3D scenes. However, this accuracy is directly linked to the precision of the ray-tracing tool used to handle the 3D.

RayBooster (http://www.hpc-sa.com) being a powerful tool, AMARTIS v2 is considered as accurate enough to perform the following simulations.

4.1. Case 1: Radiative Budget in an Urban Canyon

To illustrate the outputs of AMARTIS v2, the simulation of the observation of a canyon street pattern is detailed below. This synthetic scene consists of a street, with two buildings made of tiles (roofs) and bricks (walls), a tar road surface lined with sidewalks made of another kind of tar (Figure 7(a)). The lambertian spectral reflectances of the materials are given in appendix. The geometry and the orientation of the street are defined in Figure 7(a) and the corresponding triangular facets in Figure 7(b).

Figure 7. Synthetic urban canyon **(a)** and representation of the corresponding triangular scene facets **(b)**.

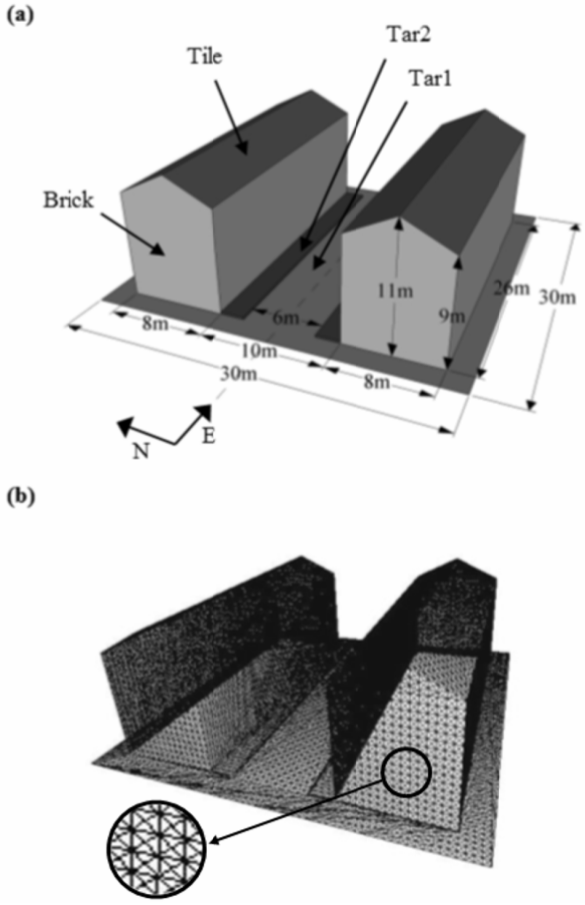

The sun has a zenith angle of 30° and an azimuth angle of 210° to the north. The airborne sensor, located at 2.4 km high, views the scene with a zenith angle of 10° and an azimuth angle of 260°. The azimuths are clockwise angles defined from the north (Figure 2). The spatial resolution of the sensor in the centre of the scene is 20 cm. The molecular atmosphere is defined by the standard "mid-latitude summer" model and the aerosols by the standard "urban" model with an abundance corresponding to a visibility of 23 km.

Figure 8. Ground irradiances **(a–d)** in $W.m^{-2}.\mu m^{-1}$ and at sensor radiances **(e–h)** in $W.m^{-2}.\mu m^{-1}.sr^{-1}$ at 670 nm.

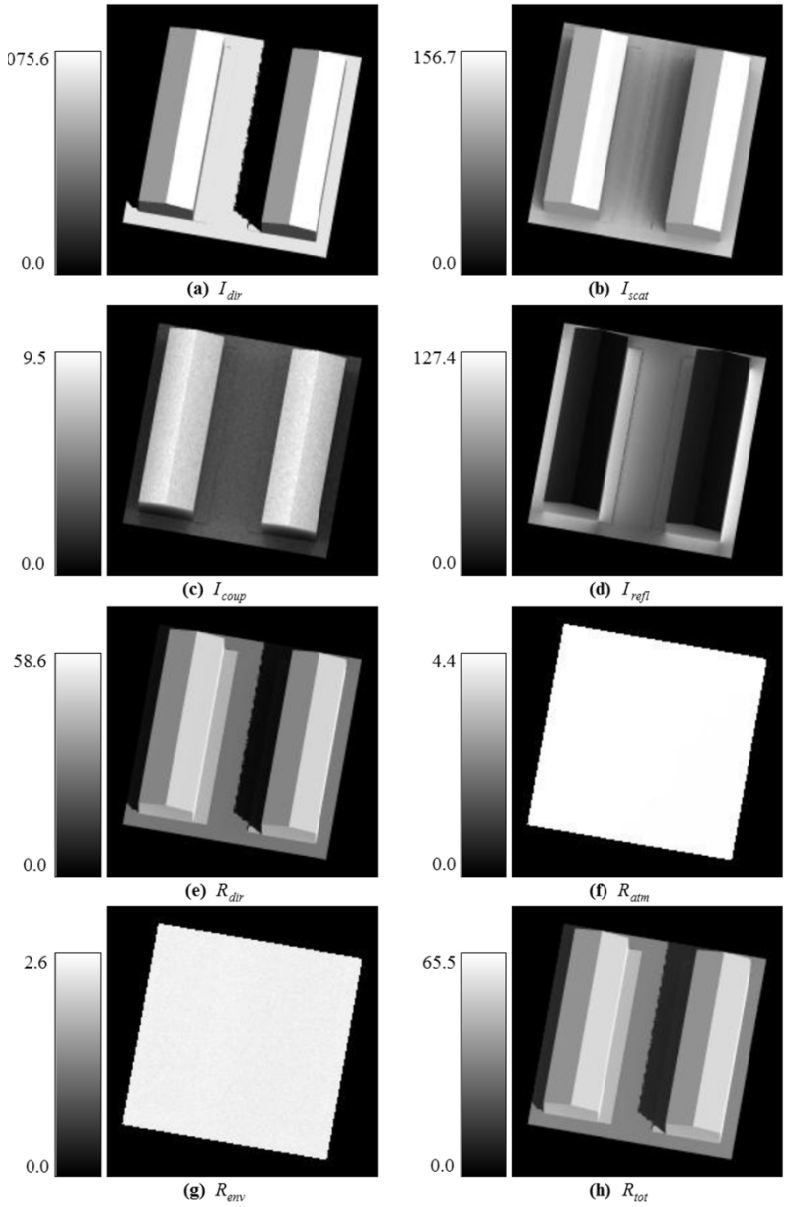

The different components of the signal, computed by AMARTIS v2 at 670 nm, are detailed in Figure 8. The direct irradiance, I_{dir}, (Figure 8(a)), has different levels due to the various slopes of the relief. In the shaded areas, this component of course equals zero. The edge of the shadow on the ground is not a straight line. This is due to the discretization of our scene description in triangular facets. The scattered irradiance, I_{scat}, (Figure 8(b)), largely varies in the scene. At street level, some sky radiance R_{sky} resulting from atmospheric scattering is screened by the buildings; this explains (*cf.* Equation (2)) the low levels of I_{scat}. Furthermore, the different levels seen on roofs are mainly due to the angular signature of the aerosol scattering which favors a forward behavior. The Earth-atmosphere coupling irradiance, I_{coup}, (Figure 8(c)), decreases from the roof to the pavement. This is mainly due to the sky viewing solid angle which limits the atmospheric contribution. Its relative contribution, at this wavelength, is very low compared to the previous components. It is interesting to note that no directional signature is observed as the multiple scatterings between the soil and the atmosphere tend

to smooth the directional behaviors of the scene and of the atmosphere. The contribution of the last irradiance, I_{refl}, (Figure 8(d)) is essentially visible on the pavements. It is quite negligible on the roofs. The dissymmetry of flux spreading on the road is due to the different impacts of facades which do not receive the same irradiation (sunny or shady). We can here notice the effect of the duplication of the scene. Indeed, for instance on the left of the image, between the building and the edge of the scene, some irradiance resulting from reflections on the building of the neighboring profile can be observed.

The direct at sensor radiance, R_{dir}, (Figure 8(e)), well takes into account the total irradiance at ground level (the two sides of the roofs correspond to different radiances and the shaded areas are clearly observed) and the materials reflectances (the radiances measured in the direction of the sidewalks and of the road are different). The atmospheric radiance, R_{atm}, (Figure 8(f)), is constant on the entire scene as it does not depend on the landscape and as the FOV of the sensor remains small. The environment radiance, R_{env}, (Figure 8(g)), is quite constant on the entire scene as the multiple scattering between the landscape and the atmosphere tends to smooth the directional behavior of the atmosphere. The results are a little bit noisy (with spatial variations of about 0.1%) as it is estimated from Monte Carlo methods but these variations are very low. At last, the total sensed radiance, R_{tot}, (Figure 8(h)), exhibits the different radiative effects in an urban canyon: slope effects, sunny and shady areas and occultations. At this wavelength and for this simulation, the main contributor is the direct component R_{dir}. R_{atm} and R_{env} have quite a similar radiative impact.

4.2. Case 2: Impact of Highly Reflective Windows

To perform materials classification from remote sensing images, the hypothesis of lambertian surfaces is usually done [8]. Nevertheless, this approximation is not always realistic [36]. Thus, it becomes necessary to model those directional behaviors when trying to estimate the signal at ground level. To this end, a window pane with a high specular behavior in an urban canyon is considered. Although this case is extreme it may be found in urban areas such as new buildings covered by metallic glass. Indeed, when a window is facing the sun, the incident solar irradiance is reflected and a highlighted footprint in a shadow might occur when this pane is characterized by a strong reflectance in the specular direction. An illustration of such effect is given in Figure 9.

Figure 9. Illustration of a very high reflection of light on windows in shadows (PELICAN image acquired over Toulouse's "Conseil Général").

The synthetic landscape used is an urban canyon whose characteristics are given in Figure 10 for its geometry and in appendix for the spectral reflectance of each material. It is modeled by two buildings made of tiles (roofs), of bricks (walls) and of windows, at both sides of a tar road surface lined with two sidewalks made of another kind of tar. All the materials have a lambertian behavior except for the windows that have a specular reflectance. This bidirectional reflectance is derived from Phong model [30]:

$$\rho^{dd}(\theta_i,\varphi_i,\theta_r,\varphi_r,\lambda) = k(\theta_i,\varphi_i,\lambda)\cos(\alpha)^n \tag{6}$$

$$\alpha = a\cos(\cos(\theta_i)\cos(\theta_r) - \sin(\theta_i)\sin(\theta_r)\cos(\varphi_r - \varphi_i)) \tag{7}$$

with ρ^{dd} the bidirectional reflectance of the window pane, (θ_i,φ_i) the incidence zenith and azimuth angles, (θ_r,φ_r) the reflection zenith and azimuth angles, and k is a normalization factor. The factor *n* in Equation (6) describes the width of the specular peak: the higher n, the narrower the peak is. As this model has no physical meaning, k is estimated by the way of its directional hemispherical reflectance *R:*

$$R(\theta_i,\lambda) = \iint_{\Omega_r} \rho^{dd}(\theta_i,\varphi_i,\theta,\varphi,\lambda)\cos(\theta)\sin(\theta)d\theta d\varphi \tag{8}$$

$$k(\theta_i,\lambda) = \frac{R(\theta_i,\lambda)}{\iint_{\Omega_r}\cos(\alpha)^n\cos(\theta)\sin(\theta)d\theta d\varphi} \tag{9}$$

The value of n has been arbitrarily fixed at 100 in order to get a very narrow peak. The values of the directional hemispherical reflectance $R(\theta_i,\lambda)$ come from measurements of a TiN coated pane published in Rubin *et al.* [37]. Note that coated panes are much more reflective than classic clear glass.

Figure 10. Description of the urban canyon.

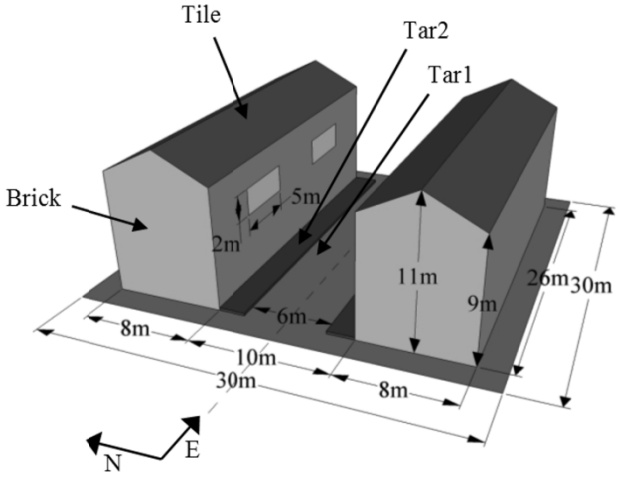

Both the sun and the sensor are located in a plan perpendicular to the street, in front of the wall with windows. The sun is located at a zenith angle of 45° and an azimuth angle of 180° (south side), whereas the sensor, located at 2.4 km high, views the scene with a zenith angle of 10° and also an azimuth angle of 180°. The atmospheric conditions are the same as in case 1.

The simulation is performed at 670 nm. The downward reflected irradiance at ground level (I_{refl}) and the simulated image (R_{tot}) are shown in Figure 11. Those components are graphed in Figure 12 for the pixels corresponding to the axis going by the two window footprint centers.

Figure 11. Downward reflected irradiance, I_{refl}, at ground level (W.m^{-2}.µm^{-1}) (**a**) and total radiance, R_{tot}, at sensor level (W.m^{-2}. sr^{-1}.µm^{-1}) (**b**).

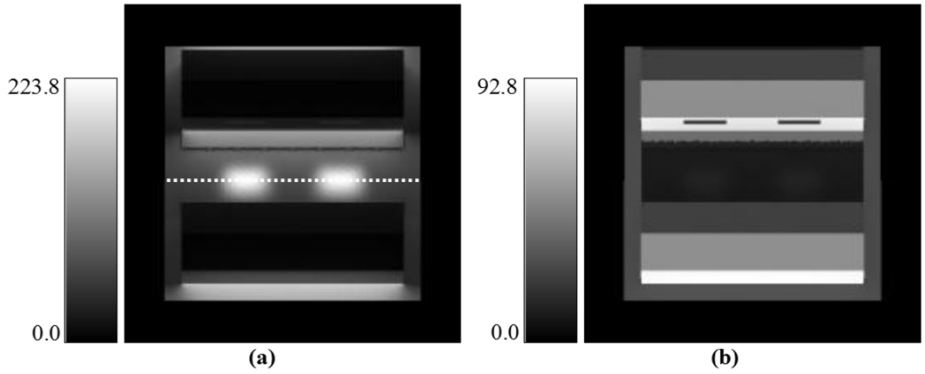

Figure 12. Downward reflected irradiance at ground level and total radiance at sensor level in the middle of the street (white line on Figure 11).

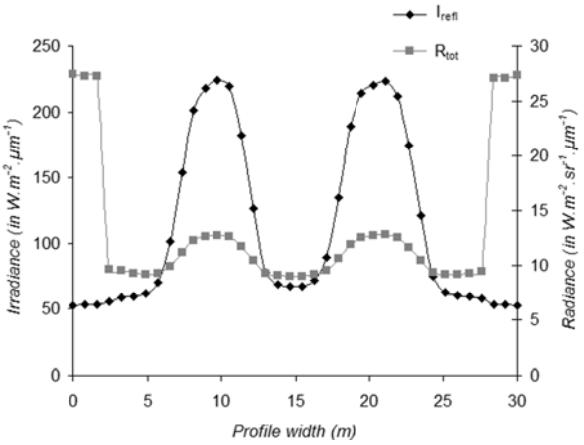

At ground level, the footprints due to the specular reflection of the windows projected to the road are clearly seen. Indeed, the maximum of downward reflected irradiance in the footprints is 224 W.m^{-2}.µm^{-1} (Figure 12) corresponding to 82% of the total irradiance, whereas outside this footprints, at street level, the downward reflected irradiance is about 67 W.m^{-2}.µm^{-1} (Figure 12), corresponding to 59% of the total irradiance.

At sensor level, the radiative impact of these footprints decreases as its relative contribution to the total signal is lower. The total radiance corresponding to a footprint is about 13 W.m^{-2}.µm^{-1}.sr^{-1}, whereas it is about 9 W.m^{-2}.µm^{-1}.sr^{-1} between the two footprints (Figure 12). The irradiance variations introduced by this specular phenomenon in regard with its close environment has a weak impact on the total sensed signal which explains why those footprints are not clearly seen on the total radiance image (Figure 11).

Furthermore, we can notice two black lines on the wall facing the sun, corresponding to the windows which do not reflect flux around the backscattering direction.

4.3. Case 3: Radiative Budget in a Crossroad in the Sun and in the Shade

The complex 3D structure of cities induces the presence of numerous shadowed areas, especially on the bottom of streets [38]. The radiative budget in shaded and irradiated areas is very different, most of

the signal received by the sensor in the first case being due to atmospheric scattering [24]. Those phenomena are crucial in remote sensing at high spatial resolution for classification works as explained previously [5]. The observation of transitions between shadowed and irradiated areas also allows retrieving information on atmospheric aerosols [17,18]. But in those two cases, preliminary phenomenological studies of the signal in the sun and in the shade are required [28]. AMARTIS v2 can be used to perform such studies. An example is given here in the case of a crossroad partially shaded.

Crossroads are typical 3D structures encountered in urban landscapes where shadows are present. This case aims to evaluate the relative amount of every radiative component in the sun and in the shade for two close points.

The geometry of the simulated crossroad is defined in Figure 13. The landscape is modeled with buildings made of tiles (roofs) and of bricks (walls), grass, and sidewalks and roads made of different tars. The corresponding lambertian spectral reflectances are given in appendix.

Figure 13. Geometry of the crossroad.

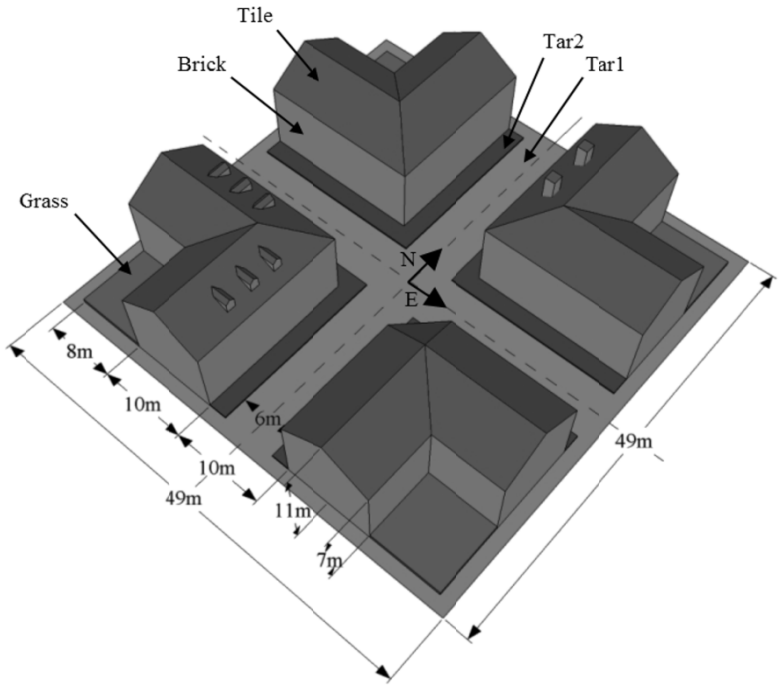

The sun is positioned in order to get a shadow in the middle of the crossroad, with a zenith angle of 55° and an azimuth angle of 150°. The airborne sensor located at 2.5 km high views the scene at nadir. The atmospheric conditions are the same as in case 1.

Simulations are performed both at 440 and 870 nm. The simulated image (R_{tot}) at 440 nm is shown in Figure 14. The total sensed radiance is shown to be varying as a function of the geometry (relief slope), of the type of materials and of the degree of irradiance (shady or sunny areas). A more accurate analysis is conducted by studying the relative contribution of the radiative terms composing the signal at bottom (for the irradiance) and at sensor (for the radiance) levels. To this end, the relative impact of every radiative component to the total signal is evaluated on two close points, one in a sunny area (point A in Figure 14) and the other in the shadow (point B in Figure 14). This analysis is achieved at two wavelengths: 440 nm (Figures 15 and 16) and 870 nm (Figure 17).

Figure 14. Total radiance at sensor level ($W.m^{-2}.\ sr^{-1}.\mu m^{-1}$) at 440 nm.

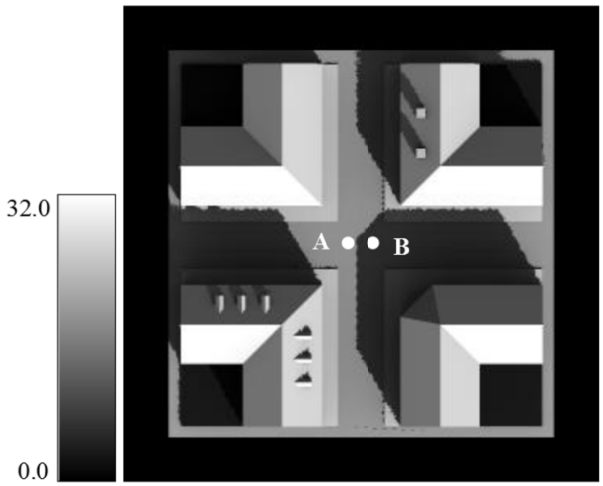

Figure 15. Relative contributions of irradiance contributors for point A in the sun (**a**) and point B in the shadow (**b**) at 440 nm.

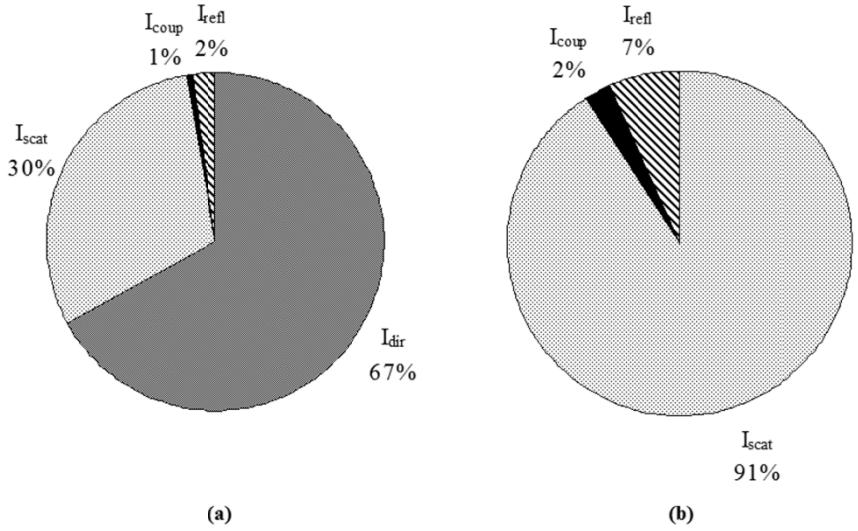

Figure 16. Relative contributions of radiance contributors at sensor level for point A in the sun (**a**) and point B in the shadow (**b**) at 440 nm.

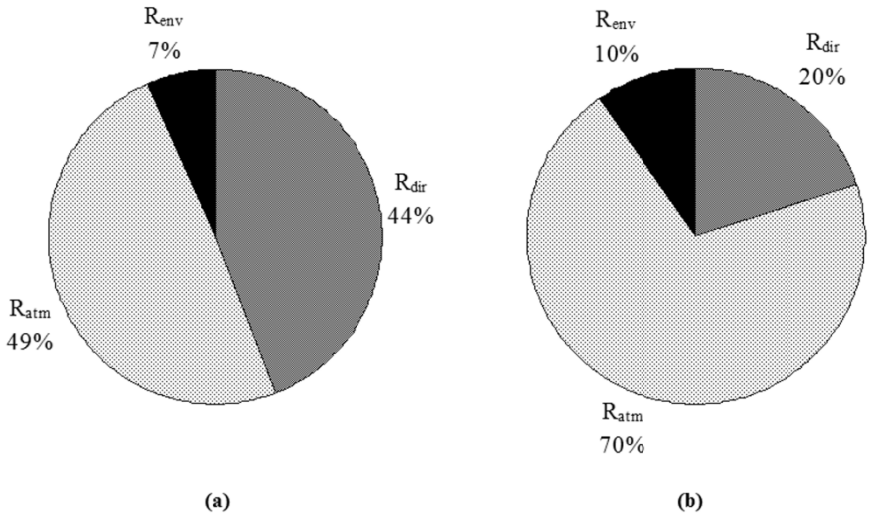

Figure 17. Relative contributions of every at-sensor radiance for point A in the sun (**a**) and point B in the shadow (**b**) at 870 nm.

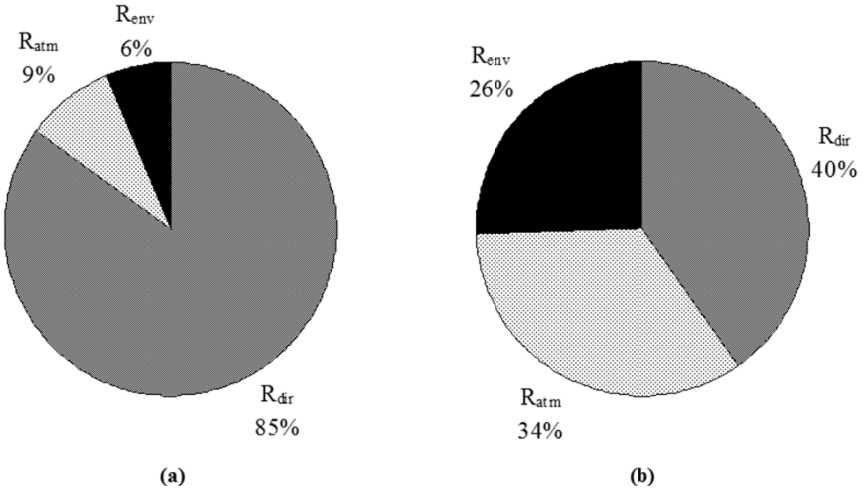

At 440 nm, the main contributor to the total irradiance (Figure 15) is the direct irradiance (67%) for point A and the scattered irradiance in the shadow (91%) for point B. We can also notice, for point A, that the scattered irradiance relative contribution also remains important (30%). The other contributors have a weak impact. On the other hand, for point B, only one irradiance (I_{scat}) dominates; the two other remaining components having a contribution of less than 10%. Nevertheless the relative impact of the reflected flux increases from 2% in the sunny area, up to 7% in the shadow.

At sensor level, in the sunny area (point A, Figure 16(a)), the two main components are the direct radiance R_{dir} with a 44% contribution and the atmospheric radiance R_{atm}, with a 49% contribution. For point B, the atmospheric radiance R_{atm} is largely dominating (70%). Furthermore, the signal characterizing the optical property of point B, R_{dir}, contributes for only 20%. As a consequence, the retrieval of urban materials reflectances in the shadows will require the atmospheric correction method with a high accuracy.

At 870 nm, the relative contributions differ. In the sunny area, the main component is now the direct radiance R_{dir} with a contribution of 85%. The other ones are weak, with less than 10% each. In the shadow, all the radiances have now a similar relative amount. Those variations are essentially due to the decrease of the atmospheric scattering when the wavelength increases, and so to the decrease of R_{atm}. The environment radiance (R_{env}) also decreases for the same reason but this decrease is partially compensated by the increase of all the materials reflectances from 440 to 870 nm (see Appendix). This component has the same absolute amount on the whole image and so contributes more in the shadows than in the sun.

4.4. Case 4: Bidirectional Effects at the Street Scale

Urban scenes are very complex landscapes as they are dominated by features of different shapes, sizes and materials. With the achievement of hyperspectral sensors dedicated to spectroscopy, improvements in urban materials classification have been made [7]. However, even with those sensors, a major limitation remains: the spatial resolution of the sensor. Indeed, the numerous types of urban materials and the spatial variations of their radiative properties [7,8,15,39] induce a majority of

non-pure pixels on the satellite and airborne remote sensing images acquired above cities, even with a high spatial resolution. Thus, Heiden *et al.* [40] estimated that more than 50% of the pixels of their HyMap images acquired over Dresden are mixed. The unmixing of urban images has become a very important issue and has been performed for several years [13,41-43]. The main drawback of these methods is that they are limited by a linear mixing assumption which is justified for flat surfaces. In fact, unmixing methods usually consider that most of the hyperspectral images are acquired with a low spatial resolution over a flat landscape in which multiple scattering of incident solar radiation can be ignored. This assumption justifies a linear mixing, the non-linear mixing being a second order effect [44]. Unfortunately, at high spatial resolution over complex landscape (vegetation or urban area) the multiple scatterings involving several materials may have a significant impact and cannot be neglected [45,46]. Thus, new unmixing procedures are required. To this end, it is necessary to understand correctly the mixing of pure materials in a pixel projected to the ground. Studies have been conducted on this subject, from the meter scale [47] to the district scale [48] for particular features. AMARTIS v2 can also be used to perform such studies as illustrated with the next example, but for any spatial resolution, any feature and any material.

This case aims to simulate the directional behavior of the at sensor signal coming from a footprint including an urban canyon (Figure 18). Thus, the radiances of every pixel i, $R_{tot,\,i}$, inside this footprint, are aggregated to obtain the aggregated radiance, R_{agg}, defined as:

$$R_{agg}(\lambda,\theta_v,\varphi_v)=\frac{\sum_i R_{tot,i}(\lambda,\theta_{v,i},\varphi_{v,i})d\omega_i}{\Omega} \tag{10}$$

where i is the pixel number, $d\omega_i$ the solid angle delimited by facet i, $R_{tot,\,i}(\lambda,\theta_{v,i},\varphi_{v,i})$ is the related total radiance emerging from pixel i in the viewing direction (zenith angle $\theta_{v,i}$ and azimuth angle $\varphi_{v,i}$) and Ω is the sum of elementary solid angles $d\omega_i$ of the pixels within area of interest.

Figure 18. Top view of the urban pattern and the related aggregated area.

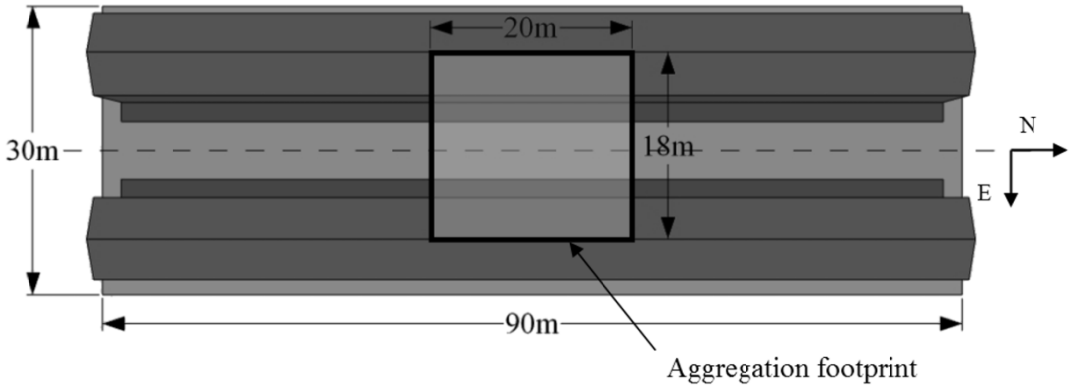

The landscape is an urban canyon, the same as in the first example but with longer buildings. Its geometry is given in Figure 18. The scene is modelled by two buildings made of tiles (roofs) and of bricks (walls), at both sides of a tar road surface lined with sidewalks made of another kind of tar. The lambertian spectral reflectances of each material are given in appendix. The aggregated area is taken in the middle of the road, between the edges of the roofs as described in the Figure 18. This area is defined at the top of the roofs.

The sun is located at an azimuth angle of 120°, and at a zenith angle of 30° for the first case and at a zenith angle of 60° for the second case. Calculations are performed for different locations of the sensor. Its zenith angles range from 0° to 60° every 15° whereas its azimuth angles range from 0 to 360° every 30°. The sensor is always looking at the scene with a resolution of 20 cm and an altitude of 2.0 km. Simulations are performed at 670 nm. The atmospheric conditions are the same as in case 1.

The bidirectional aggregated radiances of the aggregated area are shown in Figure 19. In those figures, the street is oriented to the north (0° azimuth plan).

Figure 19. Polar representations of street aggregated radiances at 670 nm where the sun is represented by a black star. The aggregated radiances given on the graphs are in $W.m^{-2}.sr^{-1}.\mu m^{-1}$. In the first case, sun zenith and azimuth angles are respectively equal to 30° and 120° (**a**) and in the second case, sun zenith and azimuth angles are respectively equal to 60° and 120° (**b**). The 0° azimuth angle points to the north.

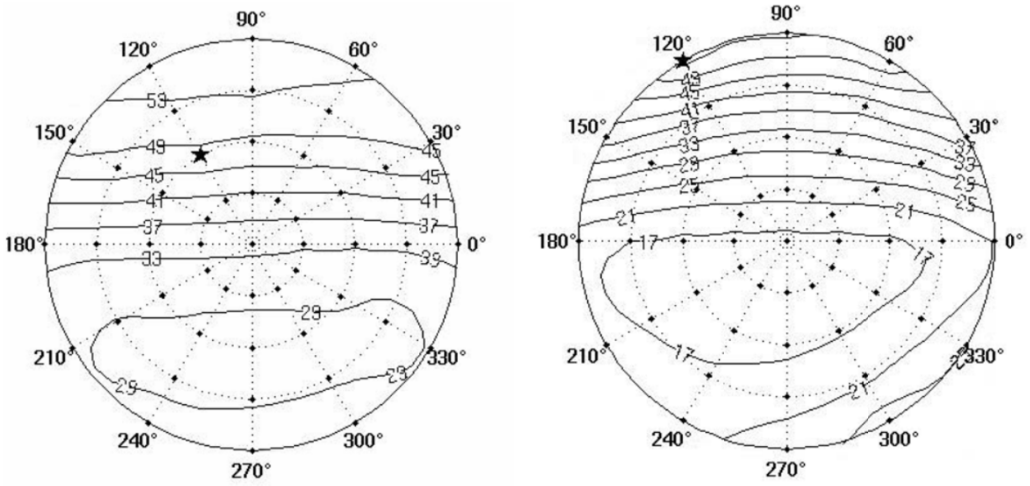

On those graphs, a characteristic signature of rough surfaces is shown: a backscattering behavior which has several origins. First, the roughness, introduced by the 3D structure, implies, for each viewing condition, that the viewed facets differ: from one viewing configuration to another, the observed facets vary in nature (materials type), in orientation and in irradiance (sunny or shady facets). Then, as the acquisitions are always done at the same height, the atmospheric transmission (respectively the atmospheric radiance) decreases (respectively increases) when the viewing zenith angle increases. These last antagonist effects tend to compensate each other.

We note that the mean radiance level is higher for a 30° solar zenith angle than for 60°. Two processes contribute to this difference. First, the smaller the solar zenith angle the larger the irradiated surfaces are. Secondly, the slopes of the roofs have an inclination angle close to 30° and then the sun irradiation is quite normal for a 30° zenith angle. The signature behavior tends to increase with the sun zenith angle.

Contrary to typical materials bidirectional reflection function, the bidirectional aggregated radiances are not symmetrical in regard to the solar plan. Indeed, the hot spot is not located in the solar direction but for a 105° azimuth angle. This is explained by the dissymmetry of the landscape in regard to the solar plan (Figure 18) [26].

5. Conclusions and Perspectives

In this paper, a new radiative transfer code is presented: AMARTIS v2. It constitutes a powerful tool to study radiative transfer in urban areas and to simulate images of urban scenes acquired by high or very high spatial resolution sensors onboard aircrafts or satellites, in the [0.4; 2.5μm] domain. It allows the simulation of all the components of the signal at ground and at sensor levels for diverse atmospheric conditions, and for various solar and viewing configurations. Complex geometries and realistic materials radiative properties (using bidirectional reflection functions, like the window pane bidirectional reflection function) can be taken into account.

This code also allows performing numerous phenomenological studies in urban areas. Indeed, as shown in this paper, this radiative transfer tool can for instance study the contribution of every component of the signal both at ground and at sensor levels. It also allows the comparison of the signal in the sunny and in the shady area of a landscape. The fourth case illustrates the aggregation process over a heterogeneous landscape. Thus, the evaluation of the introduced non-linearity in the mixing process can be evaluated which will help in the development of new non-linear unmixing methods.

Beyond those examples, this tool is very useful and efficient to develop new remote sensing methods. First, it allows the comprehension of radiative phenomena in such media [36]. Then, it can be used to compute realistic synthetic remote sensing images, whose total parameters are defined by the user, in order to test new processing methods like atmospheric characterisation, atmospheric compensation, anomaly detection or classification. This tool can obviously be used for multispectral sensors, but the monochromatic calculations performed by AMARTIS v2 makes this radiative transfer code an appropriate tool to develop applications for hyperspectral sensors. It is currently used to test a new characterization procedure of urban aerosols radiative properties based on the transitions between sunny and shady areas [17,18]. It will also be used in the near future to test the new version of ICARE (atmospheric compensation code over urban areas from hyperspectral acquisitions [5]) able to process spectral and multiangular acquisitions which might give access to walls classification and also to new unmixing methods as proposed by Zeng [49].

This code has nevertheless two drawbacks. First, it requires many input parameters to completely describe the scene, notably the complex geometry and the radiometric properties of the ground that can make the modeling of realistic scenes difficult. However, the recent efforts performed by the remote sensing community on the merging of LIDAR and hyperspectal remote sensing data allow obtaining complete characterizations of 3D complex scenes with the assessment of their spatial and spectral properties. Then, such a code is time consuming. Indeed, with the Onera's cluster dedicated to scientific calculations (64 bits cluster with 108 CPU), the AMARTIS v2 simulations last between a few minutes and a few hours. The duration of those calculations, performed without parallel processing, depends on the number of photons used for the Monte Carlo methods and on the number of facets describing the scene. For instance, the simulation of the observation of a scene of 500 m × 500 m with a spatial resolution of 1 m lasts between two and three hours.

Several points are considered to improve the performances of AMARTIS v2. First, new efforts must be done to pursue its validation. As no other radiative transfer code can both decompose the signal at ground and sensor levels and offer the modeling of complex 3D scenes, it will be necessary to validate AMARTIS v2 only on the total radiance entering the instrument. To do so, it will be possible to use

the radiative transfer code DART [23] or to use real remote sensing images, even if this case is difficult because of the impact of the instrument calibration on the radiometric quality of the data. Then, as there is a lack of bidirectional reflectance of urban material, an extensive trial will be organized in order to access a more representative optical properties data set. The main challenge is to measure these reflectances with a larger range of zenith viewing angles (from nadir up to 80°) than usual (from nadir to 60°). Such an angular range is required as would be encountered when considering a 3D landscape.

Further, in the near future, in order to improve the radiative realism of urban scenes, vegetation must be taken into account. Indeed, it seems essential to be able to model not only buildings but also 3D trees in a coming version. Finally, AMARTIS v2 will be merged with the radiative transfer code TITAN (Thermal Infrared radiance simulaTion with Aggregation modeling [50]) dedicated to the thermal infrared domain [3; 14μm]. The joint use of AMARTIS v2 and TITAN will help to accurately study the urban heat island at street and district scales and also the modeling of surface temperature.

Acknowledgments

The authors would like to thank the Jet Propulsion Laboratory, California Institute of Technology, Pasadena, California for the ASTER Spectral library.

The authors would also like to thank Didier Boldo from IGN, Florence Porez-Nadal and Philippe Lier from CNES, Sandrine Mathieu from Thales Alenia Space and Richard Santer from ULCO who have followed this study.

Appendix: Lambertian Reflectances Used in the AMARTIS v2 Computations

In this paper, 5 lambertian materials are used. Four of them, the brick modelling the walls, the two tars modelling the roads and the sidewalks, and the vegetation (grass), correspond to field measurements performed with an ASD spectrometer in the city of Toulouse during the CAPITOUL campaign [51]. The reflectance spectrum of tile, used to model the roofs, comes from the ASTER Spectral Library (http://speclib.jpl.nasa.gov). Those spectral reflectances are plotted in Figure A1.

Figure A1. Spectral lambertian reflectances of urban materials.

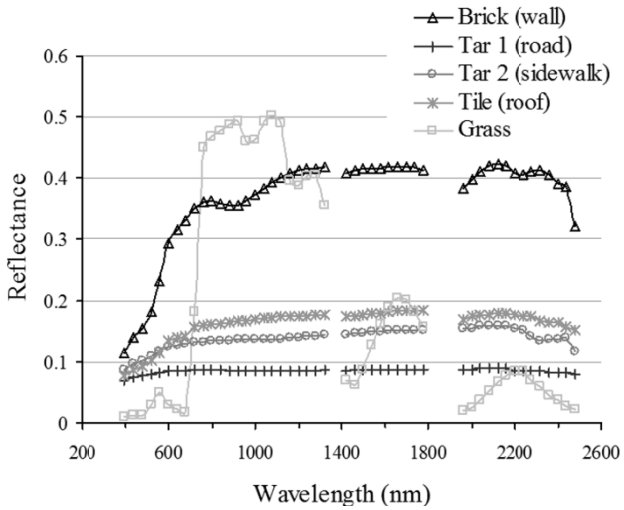

Reference

1. Weng, Q.; Quattrochi, D.A. *Urban Remote Sensing*; CRC Press, Taylor and Francis: Oxford, UK, 2006.
2. Xiao, J.; Shen, Y.; Ge, J.; Tateishi, R.; Tang, C.; Liang, Y.; Huang, Z. Evaluating urban expansion and land use change in Shijiazhuang, China, by using GIS and remote sensing. *Landscape Urban Plan.* **2006**, *75*, 69-80.
3. Miller, R.B.; Small, C. Cities from space: Potential applications of remote sensing in urban environmental research and policy. *Eviron. Sci. Policy* **2003**, *6*, 129-137.
4. Masson, V. Urban surface modeling and the meso-scale impact of cities. *Theor. Appl. Climatol.* **2006**, *84*, 35-45.
5. Lachérade, S.; Miesch, C.; Boldo, D.; Briottet, X.; Valorge, C.; Le Men, H. ICARE: A physically-based model to correct atmospheric and geometric effects from high spatial and spectral remote sensing images over 3D urban areas. *Meteorol. Atmos. Phys.* **2008**, *102*, 209-222.
6. Heiden, U.; Segl, K.; Roessner, S.; Kaufmann, H. Determination of robust spectral features for identification of urban surface materials in hyperspectral remote sensing data. *Remote Sens. Environ.* **2007**, *111*, 537-552.
7. Herold, M.; Gardner, M.E.; Noronha, V.; Roberts, D.A. Spectrometry and hyperspectral remote sensing of urban road infrastructure. *Online J. Space Commun.* **2003**, *3*, 1-29.
8. Ben-Dor, E.; Levin, N.; Saaroni, H. A spectral based recognition of the urban environment using the visible and near-infrared spectral region (0.4–1.1 μm). A case study over Tel-Aviv, Israel. *Int. J. Remote Sens.* **2001**, *22*, 2193-2218.
9. Déliot, P.; Duffaut, J.; Lacan, A. Characterization and calibration of a high resolution multi-spectral airborne digital camera. *Proc. SPIE* **2006**, *6031*, doi:10.1117/12.667894.
10. Krause, K.S. Relative radiometric characterization and performance of the QuickBird high-resolution commercial imaging satellite. *Proc. SPIE* **2004**, *5542*, doi:10.1117/12.558949.
11. Dial, G.; Bowen, H.; Gerlach, F.; Grodecki, J.; Oleszczuk, R. IKONOS satellite, imagery, and products. *Remote Sens. Environ.* **2003**, *88*, 23-36.
12. de Lussy, F.; Kubik, P.; Greslou, D.; Pascal, V.; Gigord, P.; Cantou, J.P. PLEIADES-HR Image System Products and Quality PLEIADES-HR Image System Products and Geometric Accuracy. In *Proceedings of the International Society for Photogrammetry and Remote Sensing Workshop*, Hannover, Germany, 17–20 May 2005.
13. Roessner, S.; Segl, K.; Heiden, U.; Kaufmann, H. Automated differentiation of urban surfaces based on airborne hyperspectral imagery. *IEEE Trans. Geosci. Remote Sens.* **2001**, *39*, 1525-1532.
14. Chanussot, J.; Benediktsson, J.A.; Fauvel, M. Classification of remote sensing images from urban areas using a fuzzy possibilistic model. *IEEE Geosci. Remote Sens. Lett.* **2006**, *3*, 40-44.
15. Herold, M.; Roberts, D.A.; Gardner, M.E.; Dennison, P.E. Spectrometry for urban area remote sensing—Development and analysis of a spectral library from 350 to 2,400 nm. *Remote Sens. Environ.* **2004**, *91*, 304-319.
16. Vincent, D.A.; Nielsen, K.E.; Durkee, P.A.; Reid, J.S. Aerosol Optical Depth Retrievals from High-Resolution Commercial Satellite Imagery over Areas of High Surface Reflectance. In *Proceedings of AGU Fall Meeting*, San Francisco, CA, USA, 5–9 December 2005.

17. Thomas, C.; Doz, S.; Briottet, X.; Santer, R.; Boldo, D.; Mathieu, S. Remote Sensing of Aerosols in Urban Areas: Sun/Shadow Retrieval Procedure from Airborne very High Spatial Resolution Images: First Results. In *Proceedings of the 6th EARSeL SIG IS Workshop*, Tel-Aviv, Israel, 16–19 March 2009.
18. Thomas, C.; Doz, S.; Briottet, X.; Santer, R.; Boldo, D.; Mathieu, S. Remote Sensing of Aerosols in Urban Areas: Sun/Shadow Retrieval Procedure from Airborne very High Spatial Resolution Images. In *Proceedings of the 2009 Joint Urban Remote Sensing Event*, Shanghai, China, 20–22 May 2009.
19. Vermote, E.F.; Tanre, D.; Deuzé, J.L.; Herman, M.; Morcrette, J.J. Second simulation of the satellite signal in the solar spectrum, 6S: An overview. *IEEE Trans. Geosci. Remote Sens.* **1997**, *35*, 675-686.
20. Berk, A; Anderson, G.P.; Bernstein, L.S.; Acharya, P.K.; Dothe, H.; Matthew, M.W. MODTRAN4 radiative transfer modelling for atmospheric correction. *Proc. SPIE* **1999**, *3756*, 348-353.
21. Miesch, C.; Poutier, L.; Achard, V.; Briottet, X.; Lenot, X.; Boucher, Y. Direct and inverse radiative transfer solutions for visible and near-infrared hyperspectral imagery. *IEEE Trans. Geosci. Remote Sens.* **2005**, *43*, 1552-1562.
22. Poutier, L.; Miesch, C.; Lenot, X.; Achard, V.; Boucher, Y. COMANCHE and COCHISE: Two Reciprocal Atmospheric Codes for Hyperspectral Remote Sensing. In *Proceedings of the 2002 AVIRIS Earth Science and Applications Workshop*, Pasadena, CA, USA, 5–8 March 2002.
23. Gastellu-Etchegorry, J.P.; Martin, E.; Gascon, F. DART: A 3D model for simulating satellite images and studying surface radiation budget. *Int. J. Remote Sens.* **2004**, *25*, 73-96.
24. Miesch, C.; Briottet, X.; Kerr, Y.H. Phenomenological analysis of simulated signals observed over shaded areas in an urban scene. *IEEE Trans. Geosci. Remote Sens.* **2004**, *42*, 434-442.
25. Miesch, C.; Briottet, X.; Kerr, Y.H.; Cabot. F. Monte Carlo approach for solving the radiative transfer equation over mountainous and heterogeneous areas. *Appl. Opt.* **1999**, *38*, 7419-7430.
26. Miesch, C.; Briottet, X. Bidirectional reflectance of a rough anisotropic surface. *Int. J. Remote Sens. Lett.* **2002**, *23*, 3107-4114.
27. Junge, C.E. *Air chemistry and Radiochemistry*; Academic Press: New York, NY, USA, 1963.
28. Thomas, C.; Briottet, X.; Santer, R.; Lachérade, S. Aerosols in urban areas: Optical properties and impact on the signal incident to an airborne high-spatial resolution camera. *Proc. SPIE* **2008**, *7107*, doi:10.1117/12.800001.
29. Doz, S.; Thomas, C.; Lachérade, S.; Briottet, X.; Boldo, D.; Lier, P. Simulation of High Spatial Resolution Images for Urban Remote Sensing. In *Proceedings of International Conference on Space Optics*, Toulouse, France, 14–17 October 2008.
30. Phong, B.T. Illumination for computer generated pictures. *Commun. ACM* **1975**, *18*, 311-317.
31. Cook, R.; Torrance, K. A reflectance model for computer graphics. *ACM Trans. Graph.* **1982**, *1*, 7-24.
32. Snyder, W.C.; Wan, Z. BRDF models to predict spectral reflectance and emissivity in the thermal infrared. *IEEE Trans. Geosci. Remote Sens.* **1998**, *36*, 214-225.
33. Miesch, C.; Briottet, X.; Kerr, Y.H.; Cabot, F. Radiative transfer solution for rugged and heterogeneous scene observations. *Appl. Opt.* **2000**, *39*, 6830-6846.

34. Herman, B.M.; Browning, S.R. A Numerical Solution to the equation of radiative transfer. *J. Atmos. Sci.* **1965**, *22*, 559-566.
35. Henyey, L.C.; Greenstein, J.L. Diffuse radiation in the galaxy. *Astrophs. J.* **1941**, *93*, 70-83.
36. Doz, S.; Thomas, C.; Briottet, X.; Lachérade, S. Simulation of at Sensor Signals over Urban Area: Two Cases Study. In *Proceedings of the 2009 Joint Urban Remote Sensing Event*, Shanghai, China, 20–22 May 2009.
37. Rubin, M.; Powles, R.; von Rottkay, K. Models for the angle-dependent optical properties of coated glazing materials. *Solar Energy* **1999**, *66*, 267-276.
38. Dare, P.M. Shadow analysis in high-resolution satellite imagery of urban areas. *Photogramm. Eng. Remote Sens.* **2005**, *71*, 169-177.
39. Lachérade, S.; Miesch, C.; Briottet, X.; Le Men, H. Spectral variability and bidirectional reflectance behaviour of urban materials at a 20 cm spatial resolution in the visible and near infrared wavelengths—A case study over Toulouse (France). *Int. J. Remote Sens.* **2005**, *26*, 3859-3866.
40. Heiden, U.; Roessner, S.; Segl, K.; Kaufmann, H. Analysis of Spectral Signatures of Urban Surfaces for Their Area-Wide Identification Using Hyperspectral HyMap Data. In *Proceedings of IEEE-ISPRS Joint Workshop on Remote Sensing and Data Fusion over Urban Areas*, Rome, Italy, 8–9 November 2001; pp. 173-177.
41. Ridd, M.K. Exploring a VIS (vegetation-impervious-surface-soil) model for urban ecosystem analysis through remote sensing: Comparative anatomy for cities. *Int. J. Remote Sens.* **1995**, *16*, 2165-2185.
42. Boardman, J.W.; Kruse, F.A.; Green, R.O. Mapping target signatures via partial unmixing of AVIRIS Data. In *Summaries of the Fifth JPL Airborne Earth Science Workshop*; JPL Publication 95-1; NASA: Pasadena, CA, USA, 23–26 January 1995; Volume 1, pp. 23-26.
43. Segl, K.; Roessner, S.; Heiden, U.; Kaufmann, H. Fusion of spectral and shape features for identification of urban surface cover types using reflective and thermal hyperspectral data. *ISPRS J. Photogramm. Remote Sens.* **2003**, *58*, 99-112.
44. Jia, S.; Qian, Y. Spectral and spatial complexity-based hyperspectral unmixing. *IEEE Trans. Geosci. Remote Sens.* **2007**, *45*, 3867-3879.
45. Rahman, M.T.; Alam, M.S. Nonlinear unmixing of hyperspectral data using BRDF and maximum likelihood algorithm. *Proc. SPIE* **2007**, *6566*, doi: 10.1117/12.720231.
46. Keshava, N.; Mustard, J.F. Spectral unmixing. *IEEE Signal Process. Mag.* **2002**, *19*, 44-57.
47. Meister, G.; Rothkirch, A.; Wiemker, R.; Bienlein, J.; Spitzer, H. Modeling the Directional Reflectance (BRDF) of a Corrugated Roof and Experimental Verification. In *Proceedings of IEEE International Geoscience and Remote Sensing Symposium*, Seattle, WA, USA, 6–10 July 1998; pp. 1487-1489.
48. Meister, G.; Rothkirch, A.; Spitzer, H.; Bienlein, J.K. Large-scale bidirectional reflectance model for urban areas. *IEEE Trans. Geosci. Remote Sens.* **2001**, *39*, 1927-1942.
49. Zeng, Y.; Schaepman, M.E.; Wu, B.; Clevers, J.G.P.W.; Bregt, A.K. Using Linear Spectral Unmixing of High Spatial Resolution and Hyperspectral Data for Geometric Optical Modelling. In *Proceedings of the 10th International Symposium on Physical Measurements and Spectral Signatures in Remote Sensing*, *ISPMSRS'07*, Davos, Switzerland, 12–14 March 2007.

50. Fontanilles, G.; Briottet, X.; Fabre, S.; Trémas, T. Thermal infrared radiance simulation with aggregation modeling (TITAN): An infrared radiative transfer model for heterogeneous 3-D surface—Application over urban areas. *Appl. Opt.* **2008**, *47*, 5799-5810.
51. Masson, V.; Gomes, L.; Pigeon, G.; Liousse, C.; Pont, V.; Lagouarde, J.P. The Canopy and Aerosol Particle Interactions in Toulouse Urban Layer (CAPITOUL) experiment. *Meteorol. Atmos. Phys.* **2008**, *102*, 135-157.